Inverse Problems

High-contrast impedance tomography

To cite this article: Liliana Borcea *et al* 1996 *Inverse Problems* **12** 835

View the article online for updates and enhancements.

You may also like

- Examinations of CO Completeness Based on Three Independent CO Surveys
Yan Sun, Ji Yang, Qing-Zeng Yan et al.
- Onset of thermal convection in a rectangular parallelepiped cavity of small aspect ratios
Mitsuaki Funakoshi
- Exact solution for a random walk in a time-dependent 1D random environment: the point-to-point Beta polymer
Thimothée Thiery and Pierre Le Doussal

IOP ebooks™

Bringing together innovative digital publishing with leading authors from the global scientific community.

Start exploring the collection–download the first chapter of every title for free.

This content was downloaded from IP address 141.211.4.224 on 30/12/2022 at 21:42

Inverse Problems **12** (1996) 835–858. Printed in the UK

High-contrast impedance tomography

Liliana Borcea†‖, James G Berryman‡¶ and George C Papanicolaou§+

† Scientific Computing and Computational Mathematics, Stanford University, Stanford, CA 94305, USA

‡ Lawrence Livermore National Laboratories, Earth Sciences Division, PO Box 808 L-202, Livermore, CA 94551-9900, USA

§ Department of Mathematics, Stanford University, Stanford, CA 94305, USA

Received 14 May 1996

Abstract. We introduce an output least-squares method for impedance tomography problems that have regions of high conductivity surrounded by regions of lower conductivity. The high conductivity is modelled on network approximation results from an asymptotic analysis and its recovery is based on this model. The smoothly varying part of the conductivity is recovered by a linearization process as is usual. We present the results of several numerical experiments that illustrate the performance of the method.

1. Introduction

Let Ω be a bounded two-dimensional region with conductivity $\sigma(x, y)$ and resistance (or impedance) $\rho(x, y) = 1/\sigma(x, y)$. The recovery of σ from measurements of the potential ϕ at the boundary $\partial\Omega$ is the impedance tomography problem. The potential ϕ is the solution of the boundary-value problem

$$\begin{aligned} &\nabla \cdot (\sigma \nabla \phi) = 0 \qquad \text{in } \Omega \\ &\sigma \frac{\partial \phi}{\partial n} = I \qquad \text{on } \partial\Omega \end{aligned} \tag{1.1}$$

where the imposed surface current density I satisfies $\int_{\partial\Omega} I \, \mathrm{d}S = 0$ and the potential ϕ is unique up to a constant. When the conductivity σ is sufficiently smooth and the full Neumann to Dirichlet map is known, that is, measurements of ϕ are given on $\partial\Omega$ for all possible current source distributions I, then it is known that the conductivity can be recovered in principle [29, 43, 44]. An extensive review of the uniqueness and stability of the impedance tomography problem is given in [24]. There is also an extensive literature on recovery algorithms, based mostly on linear output least-squares methods, that work well for low-contrast or linearized conductivity problems [1, 7, 17, 25, 37, 40, 42, 46]. Electromagnetic impedance tomography, in which σ in (1.1) is complex valued, is also of interest in geophysical applications [3, 4] but there is relatively little theoretical development for it at present. In this paper we consider the impedance tomography problem with static (DC) boundary excitation and real-valued conductivity. A possible configuration of current sources and points where the potential is measured, on part of the boundary of a square region, is shown in figure 1.

‖ E-mail address: borcea@sccm.stanford.edu
¶ E-mail address: berryman@s123.es.llnl.gov
+ E-mail address: papanico@math.stanford.edu

 © 1996 IOP Publishing Ltd

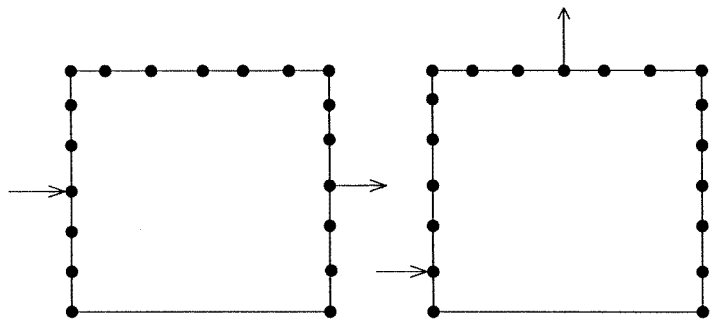

Figure 1. An impedance tomography problem for a square region Ω. Showing two current injection patterns, where the arrows represent current sources and the dots represent points where the potential is measured.

We consider the recovery of the conductivity from boundary measurements when there are regions of high contrast so that linearization methods (the Born approximation) do not work. The analysis of current flow in regions with high conductivity, the direct problem, has been carried out in [13, 30]. This analysis motivates our approach to the high-contrast inverse problem: we model the unknown conductivity in a special way, suggested by the analysis of the direct problem, and then estimate the parameters of the model conductivity by an output least-squares process.

In the next section we give a brief review of the analysis of high-contrast conductivity problems. In section 3 we describe the inversion algorithm that we use for estimating high-contrast conductivities and in section 4 we present results from numerical computations based on this algorithm. In section 5 we explain briefly why the approach we follow works. In section 6 we provide a short summary and conclusions. In the references we include several papers that are not directly related to this work but are relevant in impedance tomography.

2. The high-contrast model

2.1. Description of the model

There are many ways in which high-contrast conductivity may arise in practice. We can have, for example, a uniform background conductivity with highly conducting or insulating inclusions. Since in most potential applications we do not know the shape of the inclusions, it is convenient to assume that the high contrast of the conductivity (σ) arises in a general way from a continuum model of the form

$$\sigma(\boldsymbol{x}) = \sigma_0 \, \mathrm{e}^{-S(\boldsymbol{x})/\epsilon}. \tag{2.1}$$

Here σ_0 is a constant reference conductivity, $S(\boldsymbol{x})$ is a smooth function and ϵ is a small parameter. Variations of the function $S(\boldsymbol{x})$, the scaled logarithm of the conductivity, are amplified by the parameter ϵ, producing the high contrast of the conductivity. Media with discontinuous conductivities, like ones with inclusions of finite size, can then be viewed as particular cases of the generic model (2.1).

2.2. Review of the asymptotic theory

In this section we review some of the results obtained in [13, 30] for transport in media with high-contrast conductivity given by (2.1). Even though the analysis is done in the context of homogenization [8, 26] the conclusions are equally valid for more general circumstances.

We consider the flow problem

$$\nabla \cdot (\sigma \nabla \phi) = 0 \tag{2.2}$$

in a periodic unit cell Ω, where ϕ is the electric potential and $\sigma(\boldsymbol{x})$ is the conductivity. The flow is driven by the condition

$$\langle \nabla \phi \rangle = \boldsymbol{e} \tag{2.3}$$

where $\langle \cdot \rangle$ stands for the normalized average over Ω and $\boldsymbol{e}$ is a unit vector. The mean potential gradient can be specified, for example, by prescribing two different constant potentials at opposite sides of the domain.

By using Ohm's law $\boldsymbol{j} = \sigma \nabla \phi$, where $\boldsymbol{j}$ is the electric current, we can also consider the dual problem

$$\begin{aligned} &\nabla \times (\rho \boldsymbol{j}) = 0 \\ &\nabla \cdot \boldsymbol{j} = 0 \\ &\langle \boldsymbol{j} \rangle = \boldsymbol{e} \end{aligned} \tag{2.4}$$

where $\rho(\boldsymbol{x}) = \sigma(\boldsymbol{x})^{-1}$ is the resistance.

It is shown in [13, 30] that when the conductivity has logarithmic high contrast in the form (2.1) there is strong channelling of the flow at the saddle points of σ. Moreover, by using the variational formulation of the effective conductivity and resistance [13]

$$\begin{aligned} \bar{\sigma} &= \min_{\langle \nabla \phi \rangle = e} \langle \sigma \nabla \phi \cdot \nabla \phi \rangle \\ \bar{\rho} &= \frac{1}{\bar{\sigma}} = \min_{\langle \boldsymbol{j} \rangle = e, \nabla \cdot \boldsymbol{j} = 0} \langle \rho \boldsymbol{j} \cdot \boldsymbol{j} \rangle \end{aligned} \tag{2.5}$$

it is shown that, in the asymptotic limit of high contrast, the leading-order term in the effective parameters $\bar{\sigma}$ and $\bar{\rho}$ is obtained by considering the flow only in the neighbourhoods of the saddle points of σ.

To explain this flow behaviour in the vicinity of the saddles, let us assume that the conductivity has a single saddle point $\boldsymbol{x}_S \in \Omega$, which is oriented in the driving direction, say $\boldsymbol{e} = \boldsymbol{e}_1 = (1, 0)$. In a small neighbourhood of $\boldsymbol{x}_S$, the conductivity has the form

$$\sigma(\boldsymbol{x}) \approx \sigma(\boldsymbol{x}_S) \exp\left[\frac{k(x - x_S)^2}{2\epsilon} - \frac{p(y - y_S)^2}{2\epsilon}\right] \tag{2.6}$$

where k and p are the curvatures of $S(\cdot)$ at the saddle point. In general, the saddle point can be oriented in any direction but equation (2.6) still holds if, at $\boldsymbol{x}_S$, we introduce a local system of coordinates (x, y) such that the x direction coincides with the direction of the saddle. We take as the small region around $\boldsymbol{x}_S$ the square $| x - x_S | \leqslant \delta, | y - y_S | \leqslant \delta$ where the parameter $\delta \to 0$ in such a way that $\delta/\epsilon \to \infty$ as $\epsilon \to 0$.

From (2.2), the local problem near the saddle point is

$$\begin{aligned} &\nabla \cdot \left\{ \sigma(\boldsymbol{x}_S) \exp\left[\frac{k(x - x_S)^2}{2\epsilon} - \frac{p(y - y_S)^2}{2\epsilon}\right] \nabla \phi \right\} = 0 \\ &\langle \nabla \phi \rangle = \boldsymbol{e}_1 \end{aligned} \tag{2.7}$$

which we solve by separation of variables. The potential $\phi(\boldsymbol{x})$ is

$$\phi(x, y) \approx \frac{1}{2}\mathrm{erf}\left(\sqrt{\frac{k}{2\epsilon}}(x - x_S)\right) \tag{2.8}$$

correct up to an additive constant which is set to zero here. The analytical basis for (2.8) is matched asymptotic expansions. The local analysis gives the leading term (2.8) of the inner expansion valid near the saddle point. The outer expansion deals with the diffuse flow in the rest of the domain. The potential $\phi(\boldsymbol{x})$, therefore, has the character of an inner layer in the direction of the saddle, the x direction in this case.

From (2.8) we compute the potential gradient

$$\nabla\phi(x, y) \approx \frac{1}{\sqrt{2\pi\epsilon/k}}\ \mathrm{e}^{-k(x-x_S)^2/2\epsilon}\boldsymbol{e}_1 \tag{2.9}$$

and the current

$$\boldsymbol{j} = -\sigma\nabla\phi \approx -\frac{\sigma(\boldsymbol{x}_S)}{\sqrt{2\pi\epsilon/k}}\ \mathrm{e}^{-p(y-y_S)^2/2\epsilon}\boldsymbol{e}_1. \tag{2.10}$$

We see from these expressions that when the contrast of σ is high (ϵ is small) both the current and the potential gradient are narrow Gaussians centred at $\boldsymbol{x}_S$, which means that there is strong flow channelling around the saddle point of the conductivity. The results (2.9) and (2.10) imply that the overall, or effective, conductivity and resistance (2.5) are (see [13, 30])

$$\bar{\sigma} \approx \sigma(\boldsymbol{x}_S)\sqrt{\frac{k}{p}} \qquad \text{and} \qquad \bar{\rho} \approx \frac{1}{\sigma(\boldsymbol{x}_S)}\sqrt{\frac{p}{k}}. \tag{2.11}$$

Thus, the flow through a medium with high-contrast conductivity can be approximated by the flow through a resistor having resistance $\bar{\rho}$, given by (2.11).

In more general situations, where there are more saddle points of σ in the region that are oriented in different directions, the flow still concentrates at the saddles but it follows a more complicated pattern, which is a network of channels. Locally, around each saddle point of the conductivity, the flow is approximated by the current through resistors given by (2.11). These resistors are connected in a network that is identified as follows: the nodes of the network are the maxima of $\sigma(\boldsymbol{x})$ and the branches are paths connecting two adjacent maxima over a saddle point. A detailed analysis is given in [13].

3. Inversion algorithm

The asymptotic network theory described in section 2 suggests that if we have flow channelling in the medium that we are trying to image, there is significant information in the data about the resistor network that describes the flow in the high-contrast regions of the conductivity. Thus, in the first step of the inversion algorithm, we should attempt to identify the resistor network (channels of flow). The flow through this network is also the leading-order term of the flow in the high-contrast regions of σ. We can then use the conductivity estimate from the first stage of the inversion algorithm as a starting point for the second stage, in which we try to recover other features that were not captured by the network. In this step of the inversion we can linearize about the conductivity of the resistor network. Linearization works well at this stage because the main part of the flow through the high-contrast regions of σ is already estimated, and small changes of the conductivity about it produce only small changes in the potential gradients.

3.1. Identification of the asymptotic resistor network

In order to identify the resistor network that describes the flow through the high-contrast regions, we *model* the unknown conductivity σ by

$$\sigma(\boldsymbol{x}) \longrightarrow \sigma_{\mathrm{b}} + \sum_{j=1}^{m} \chi_j(\boldsymbol{x}, \boldsymbol{s}_j) f_j(\boldsymbol{x}, \boldsymbol{s}_j). \tag{3.1}$$

Here σ_{b} is a uniform background in which we imbed the high-contrast modules $f_j(\cdot)$. Each high-contrast module is of the form $f_j(\cdot) \sim \mathrm{e}^{S_j(\boldsymbol{x})/\epsilon}$, with support in the interior of Ω, and consists of a saddle point surrounded by two maxima and two minima. The vectors of parameters $\boldsymbol{s}_j$ describe the structure of the modules $f_j(\cdot)$ by specifying the position of the saddle points, their orientation, the curvatures at the saddle, the contrast, etc. The modules $f_j(\cdot)$ are localized with the smooth cut-off functions $\chi_j(\cdot)$. Detailed descriptions are given in section 4.2.

Since conductivities defined by (3.1) are completely determined by the parameters $\boldsymbol{s}_j$, $j = 1, \ldots, m$, we estimate them by minimizing the error between the solution with these parameters and the observed data. Thus, we estimate the $\boldsymbol{s}_j$, $j = 1, \ldots, m$ by minimizing the mean-square error

$$E(\boldsymbol{s}_1, \ldots, \boldsymbol{s}_m) = \sum_{i=1}^{M} \sum_{k=1}^{N} [\psi_k^{(i)} - \phi_k^{(i)}(\boldsymbol{s}_1, \ldots, \boldsymbol{s}_m)]^2 \tag{3.2}$$

where the index of summation k runs through the data points on the boundary and i labels the pair of electrodes at which the current is injected into the domain. The potential measured on the boundary is $\psi_k^{(i)}$, while $\phi_k^{(i)}(\cdot)$ is the potential on the boundary calculated by solving the partial differential equation (1.1) with the current best estimate of a conductivity of the form (3.1). This is an output least-squares estimation method, parametrized with high-contrast conductivities of the form (3.1).

Introducing a model of the form (3.1) for the conductivity is a form of *regularization* [32, 34, 35, 45] for the output least-squares problem (3.2). It is particularly well suited to high-contrast problems, as we know from the analysis of the direct problem summarized in section 2.2.

To describe the minimization algorithm that we use, we assume for simplicity that we have only one high-contrast module ($m = 1$) in (3.1). When the vector of parameters $\boldsymbol{s} \in \mathbb{R}^p$ changes by $\Delta\boldsymbol{s}$, the mean-square error (3.2) changes by

$$E(\boldsymbol{s}) + \Delta E \approx \sum_{i=1}^{M} \sum_{k=1}^{N} \left[\psi_k^{(i)} - \phi_k^{(i)}(\boldsymbol{s}) - \sum_{j=1}^{p} \frac{\partial \phi_k^{(i)}}{\partial s_j} \Delta s_j \right]^2 \tag{3.3}$$

where we use the fact that, when the change in $\boldsymbol{s}$ is small, we have

$$\phi_k^{(i)}(\boldsymbol{s} + \Delta\boldsymbol{s}) \approx \phi_k^{(i)}(\boldsymbol{s}) + \sum_{j=1}^{p} \frac{\partial \phi_k^{(i)}}{\partial s_j} \Delta s_j. \tag{3.4}$$

From (3.3) the change in the error is

$$\Delta E \approx \sum_{j=1}^{p} \sum_{l=1}^{p} A_{jl} \Delta s_j \Delta s_l - 2 \sum_{j=1}^{p} b_j \Delta s_j. \tag{3.5}$$

Here we introduced the symmetric positive definite sensitivity matrix

$$A_{jl} = \sum_{i=1}^{M} \sum_{k=1}^{N} \frac{\partial \phi_k^{(i)}}{\partial s_j} \frac{\partial \phi_k^{(i)}}{\partial s_l} \tag{3.6}$$

and the vector

$$b_j = \sum_{i=1}^{M}\sum_{k=1}^{N}[\psi_k^{(i)} - \phi_k^{(i)}(\boldsymbol{s})]\frac{\partial \phi_k^{(i)}}{\partial s_j} \tag{3.7}$$

whose components measure the current data misfit weighted by the sensitivity of the potential to changes in s_j. The decrease in the error ΔE is maximized when the parameters $\Delta \boldsymbol{s}$ satisfy the linear equations

$$\mathbf{A}\Delta \boldsymbol{s} = \boldsymbol{b} \tag{3.8}$$

and then the change in the mean-square error is

$$\Delta E \approx -\Delta \boldsymbol{s}^{\mathrm{T}}\mathbf{A}\Delta \boldsymbol{s} \leqslant 0. \tag{3.9}$$

This Gauss–Newton algorithm [18, 20, 21], given by (3.6)–(3.8), does not work well here because the matrix $\mathbf{A}$, defined by (3.6), is ill-conditioned. Some of the components of the parameter vector $\boldsymbol{s}$ change faster than others. For example, when the contrast is high and the flow concentration at the saddle point is strong, the position of the saddle point is recovered after a few iterations while the contrast converges slowly. We avoid this difficulty by updating the vector of parameters $\boldsymbol{s}$ one component at a time, instead of all at once. This approach has, in addition, the advantage of allowing us to terminate the updating of parameters that have converged before the end of the overall iteration process. The change in the jth component of $\boldsymbol{s}$ that maximizes the decrease in the error is easily found to be

$$\Delta s_j = \frac{\sum_{i=1}^{M}\sum_{k=1}^{N}[\psi_k^{(i)} - \phi_k^{(i)}(\boldsymbol{s})](\partial \phi_k^{(i)}/\partial s_j)}{\sum_{i=1}^{M}\sum_{k=1}^{N}(\partial \phi_k^{(i)}/\partial s_j)^2} = \frac{b_j}{A_{jj}} \tag{3.10}$$

and then

$$\Delta E \approx -(\Delta s_j)^2 \sum_{i=1}^{M}\sum_{k=1}^{N}\left(\frac{\partial \phi_k^{(i)}}{\partial s_j}\right)^2 = -A_{jj}(\Delta s_j)^2 \leqslant 0. \tag{3.11}$$

The change in the parameters $\boldsymbol{s}$ depends both on the error at the boundary and on the sensitivity coefficients $\partial \phi_k^{(i)}/\partial s_j$. Thus, at each step of the iteration we must solve the elliptic problems

$$\nabla \cdot (\sigma \nabla \phi) = 0 \qquad \sigma \frac{\partial \phi}{\partial n} = f \qquad \text{on} \qquad \partial\Omega \qquad \phi(\mathbf{0}, \boldsymbol{s}) = 0 \tag{3.12}$$

and

$$\begin{aligned} &\nabla \cdot \left(\sigma \nabla \frac{\partial \phi}{\partial s_i}\right) = -\nabla \cdot \left(\frac{\partial \sigma}{\partial s_i}\nabla \phi\right) \\ &\sigma \frac{\partial}{\partial n}\left(\frac{\partial \phi}{\partial s_i}\right) = 0 \qquad \text{on} \qquad \partial\Omega \\ &\frac{\partial \phi}{\partial s_i}(\mathbf{0}, \boldsymbol{s}) = 0 \qquad \text{for} \qquad i = 1, \ldots, p. \end{aligned} \tag{3.13}$$

However, since small changes in the components of $\boldsymbol{s}$ lead to an updated potential of the form (3.4), we need not solve (3.12) for each iteration but only once every p iterations.

In the Gauss–Newton method used here we approximate the Hessian of the mean-square error (3.1) by the first derivatives of the estimated potential (3.4). We omit the second derivatives which are difficult to calculate. The success of the method depends on the negligibility of second derivatives [18, 20, 21] and to insure that they are negligible, we scale the update in the parameters (3.10) by a factor $\lambda_c > 0$. The algorithm then called a damped Gauss–Newton method [18, 21] is globally convergent for many nonlinear

least-squares problems, including large residual problems [18, 21]. In our computations we choose the scaling parameter λ_c so that the change in s_j is smaller than 15%.

3.2. Identification of features of the conductivity that are neglected by the asymptotic theory

The resistor network identified by the algorithm described in section 3.1 is in general only a rough estimate of the conductivity $\sigma(\boldsymbol{x})$. In order to improve its resolution we must also identify low-contrast features of $\sigma(\boldsymbol{x})$ that are not captured by the asymptotic resistor network theory. This is done by linearizing about the network conductivity estimated by the algorithm described in the previous section. In this section we define the linearized problem and explain why it works at this stage of the inversion algorithm.

For a reference medium with conductivity $\sigma_r(\boldsymbol{x})$ of form (3.1), we have

$$\begin{aligned} &\nabla \cdot [\sigma_r(\boldsymbol{x})\nabla\phi_r(\boldsymbol{x})] = 0 \qquad \text{in} \qquad \Omega \\ &\sigma_r \frac{\partial \phi_r}{\partial n} = I \qquad \text{on} \qquad \partial\Omega \end{aligned} \tag{3.14}$$

where $\phi_r(\boldsymbol{x})$ is the reference potential. Suppose that

$$\sigma(\boldsymbol{x}) = \sigma_r(\boldsymbol{x}) + \delta\sigma(\boldsymbol{x}) \qquad \text{where } |\,\delta\sigma(\boldsymbol{x})\,| \ll |\,\sigma_r(\boldsymbol{x})\,| \,. \tag{3.15}$$

Then problem (1.1) can be written as

$$\begin{aligned} &\nabla \cdot [\sigma_r(\boldsymbol{x})\nabla\psi(\boldsymbol{x})] = -\nabla \cdot [\delta\sigma(\boldsymbol{x})\nabla\phi(\boldsymbol{x})] \qquad \text{in} \qquad \Omega \\ &(\sigma + \delta\sigma)\frac{\partial \phi}{\partial n} = I \qquad \text{on} \qquad \partial\Omega \end{aligned} \tag{3.16}$$

where $\psi(\boldsymbol{x}) = \phi(\boldsymbol{x}) - \phi_r(\boldsymbol{x})$. The perturbed potential gradient $\nabla\psi(\boldsymbol{x})$ that is due to the change $\delta\sigma(\boldsymbol{x})$ of the reference conductivity is assumed to be much smaller than the reference potential gradient $\nabla\phi_r(\boldsymbol{x})$, so we linearize (3.16)

$$\nabla \cdot [\sigma_r(\boldsymbol{x})\nabla\psi(\boldsymbol{x})] \approx -\nabla \cdot [\delta\sigma(\boldsymbol{x})\nabla\phi_r(\boldsymbol{x})] \qquad \text{in} \qquad \Omega. \tag{3.17}$$

Equation (3.17) is linear in $\delta\sigma(\boldsymbol{x})$. Linearization is justified in the second stage of our inversion algorithm because, as we explained in section 2.2, the resistor network given by $\sigma_r(\boldsymbol{x})$ determines the main part of the flow in the high-contrast regions of the medium. Small changes of the reference conductivity can only produce small changes in the potential gradient, so linearization (3.17) can be used.

Inversion of the linearized problem (3.17), that is recovery of $\delta\sigma(\boldsymbol{x})$, has been the topic of numerous studies and an extensive literature on recovery algorithms is available [1, 7, 17, 25, 37, 40, 42, 46]. In our computations we used an adjoint representation [39] that requires less computation than the usual algorithms that are based on Green functions.

4. Numerical results

4.1. The PLTMG solver

We review a few facts about the software package PLTMG [5] that we use for solving the elliptic problems (3.12) and (3.14) during the iterative process described in section 3. PLTMG is an elliptic partial differential equation solver in two dimensions. It uses an adaptive multigrid approach and a finite-element discretization based on continuous piecewise linear triangular elements.

We extensively tested the performance of PLTMG for problems of form (3.12) with high-contrast conductivity in [14]. We found that for contrasts no higher than $O(10^2)$, the

numerical solution given by PLTMG is accurate, within a few per cent. When the contrast is higher, the solution produced by PLTMG can be quite inaccurate in the vicinity of the saddle points of σ where strong flow channelling occurs, but overall remains satisfactory away from the channels. Since in our computations we use only the boundary values of the potential and we assume that all the channels are in the interior of Ω, we may use PLTMG for computing the potential $\phi(\boldsymbol{x}, \boldsymbol{s})$ and the sensitivity coefficients $\partial\phi(\boldsymbol{x}, \boldsymbol{s})/\partial s_i$, $i = 1, \ldots, p$, on the boundary.

4.2. One-channel model

In this section we present numerical results obtained with the inversion algorithm described in section 3 for conductivities that have only one saddle point in the domain. An example of such a conductivity is

$$\sigma(\boldsymbol{x}) = \sigma_{\mathrm{b}} + \chi(\boldsymbol{x}, \boldsymbol{s}) f(\boldsymbol{x}, \boldsymbol{s}) \tag{4.1}$$

where σ_{b} is a uniform background $f(\cdot)$ is a high-contrast module that has a saddle point surrounded by two maxima and two minima and $\chi(\cdot)$ is a cut-off function that localizes $f(\cdot)$. We model the high-contrast module by

$$f(\boldsymbol{x}, \boldsymbol{s}) = \sigma_0 \exp\left\{\frac{1}{\epsilon}\sin[\alpha((x - x_{\mathrm{s}})\cos\theta + (y - y_{\mathrm{s}})\sin\theta)] \times \sin[\beta((y - y_{\mathrm{s}})\cos\theta - (x - x_{\mathrm{s}})\sin\theta)]\right\} \tag{4.2}$$

where $(x_{\mathrm{s}}, y_{\mathrm{s}})$ is the location of the saddle point of the conductivity, θ is the orientation of the saddle and ϵ determines the contrast. The function $f(\cdot)$ in (4.2) is periodic with periods determined by α and β, which also determine the curvatures at the saddle. The constant σ_0 controls the height of the saddle. Thus, the high-contrast conductivity module is completely described by the eight-component vector

$$\boldsymbol{s} = (\sigma_{\mathrm{b}}, \sigma_0, \alpha, \beta, x_{\mathrm{s}}, y_{\mathrm{s}}, \theta, \epsilon). \tag{4.3}$$

The high-contrast module $f(\cdot)$ is tapered with the C^1 cut-off function

$$\chi(\boldsymbol{x}, \boldsymbol{s}) = g((x - x_{\mathrm{s}})\cos\theta + (y - y_{\mathrm{s}})\sin\theta, \alpha) g(-(x - x_{\mathrm{s}})\sin\theta + (y - y_{\mathrm{s}})\cos\theta, \beta) \tag{4.4}$$

where

$$g(\xi, \gamma) = \begin{cases} \sin^3[(\pi/2)(\xi + (\pi/\gamma))/d] & \text{for } -\pi/\gamma \leqslant \xi \leqslant -\pi/\gamma + d \\ -\sin^3[(\pi/2)(\xi - (\pi/\gamma))/d] & \text{for } \pi/\gamma - d \leqslant \xi \leqslant \pi/\gamma \\ 1 & \text{for } -\pi/\gamma + d \leqslant \pi/\gamma - d \\ 0 & \text{for } |\xi| \geqslant \pi/\gamma. \end{cases} \tag{4.5}$$

The parameter d in (4.5) controls the sharpness of the cut-off and it is kept constant throughout the numerical experiments.

The data that we use in the numerical experiments are generated numerically with a synthetic model of the form (4.1) and PLTMG. An example of a conductivity used to generate data is shown in figure 2. In a uniform background, $\sigma_{\mathrm{b}} = 2$, we have embedded a high-contrast module ($\max(\sigma)/\min(\sigma) = 369$) that has a saddle at $(x_{\mathrm{s}}, y_{\mathrm{s}}) = (0.3, 0.4)$ which is oriented at an angle $\pi/4$ from the axes.

As a starting point in the iterative process of reconstructing the model σ shown in figure 2, we consider the conductivity shown in figure 3. Even though the initial guess is of the same form (4.1) as the model, the set of parameters $\{\boldsymbol{s}\}$ describing it is very different.

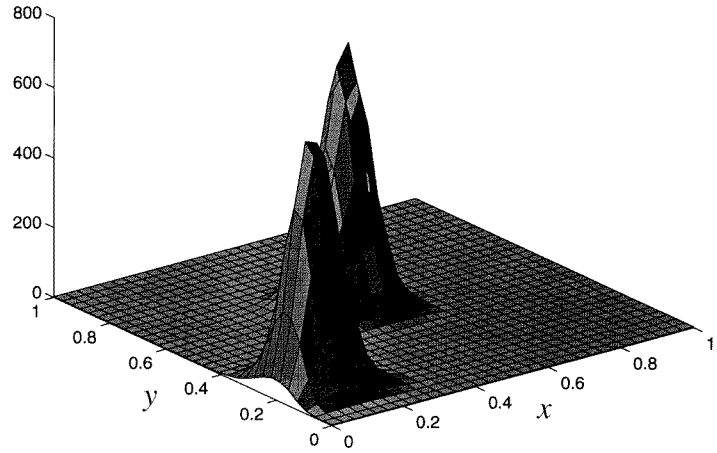

Figure 2. Model conductivity (contrast = 369).

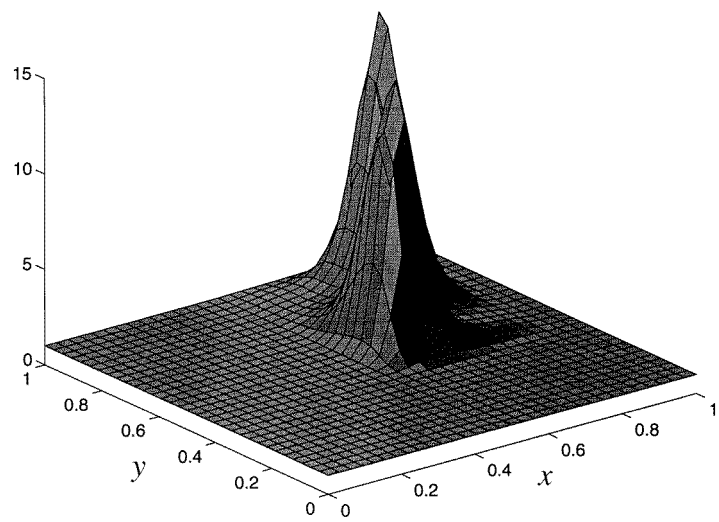

Figure 3. Initial conductivity guess (contrast = 14.7).

The background conductivity is $\sigma_b^{init} = 1$, the saddle is situated at $(x_s, y_s)^{init} = (0.7, 0.7)$ and the contrast is 14.7. The initial relative error in the conductivity (see figure 4) is very high around the initial guess of the position of the saddle ($\sim$ 600%) and about 60% elsewhere in the domain.

In the reconstruction process, the data consist of the value of the potential at points placed a distance $h = 1/32$ apart along the sides ($x = 0$ and $x = 1$) and the surface boundary ($y = 1$). Current is injected with two different pairs of electrodes located at (0, 0.5), (1, 0.5) and (0, 0.3), (0.5, 1), respectively.

The evolution of the mean-square data error during the iteration process is shown in figure 5. The algorithm reduces this error monotonically. However, it does not guarantee reduction of the error in the conductivity as shown in figure 6. At some stage of the iteration process the error in the model actually increases. This behaviour is due to the

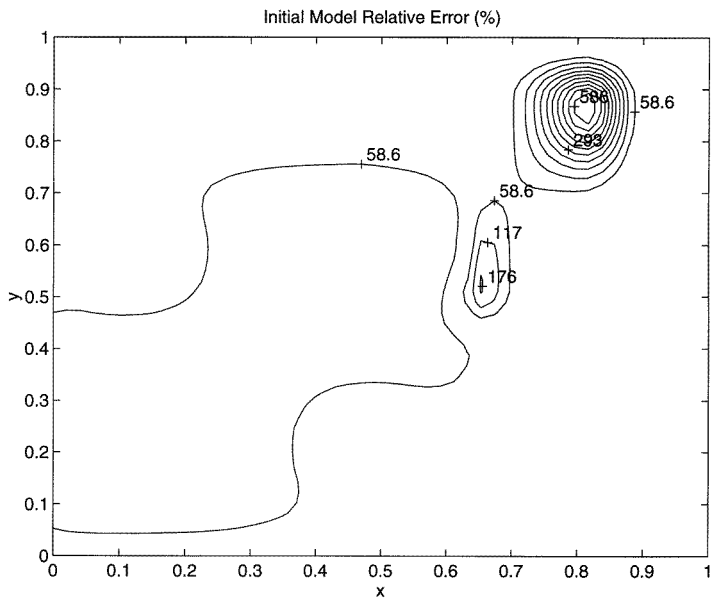

Figure 4. L_∞ initial relative error in the conductivity.

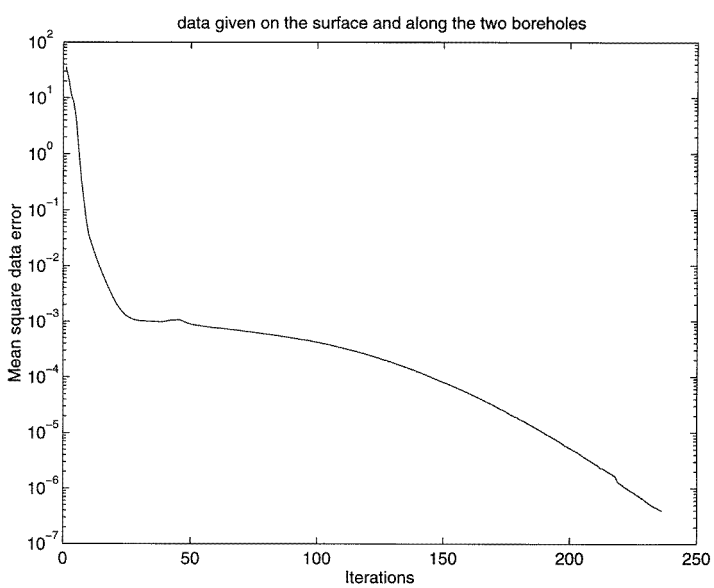

Figure 5. Evolution of the mean-square data error.

strong nonlinearity of the problem and is more subdued in experiments with contrast of order ten. After 250 iterations, the relative error in the conductivity in the L_2 norm is reduced by two orders of magnitude. The final relative error in the model in the L_∞ norm (see figure 7) is only a few per cent so the model conductivity is recovered quite well.

During the reconstruction process, some of the components of the vector of parameters $\boldsymbol{s}$ describing the model conductivity are recovered more quickly than others. For example,

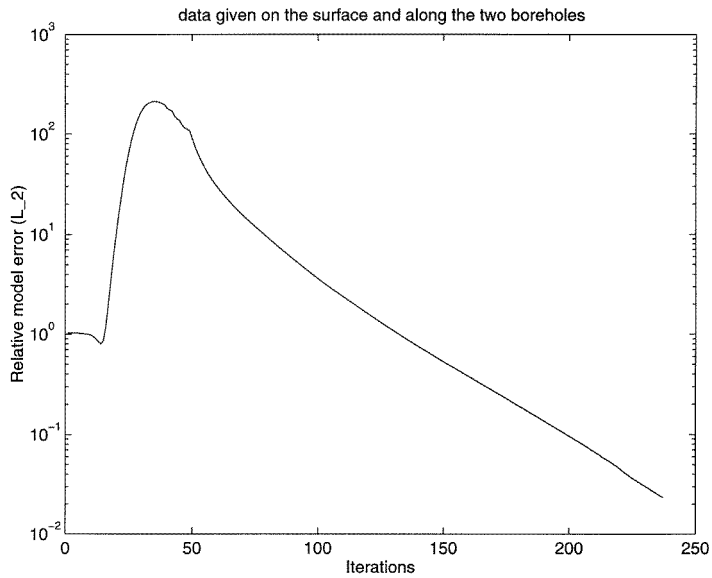

Figure 6. Evolution of the L_2 relative error in the conductivity.

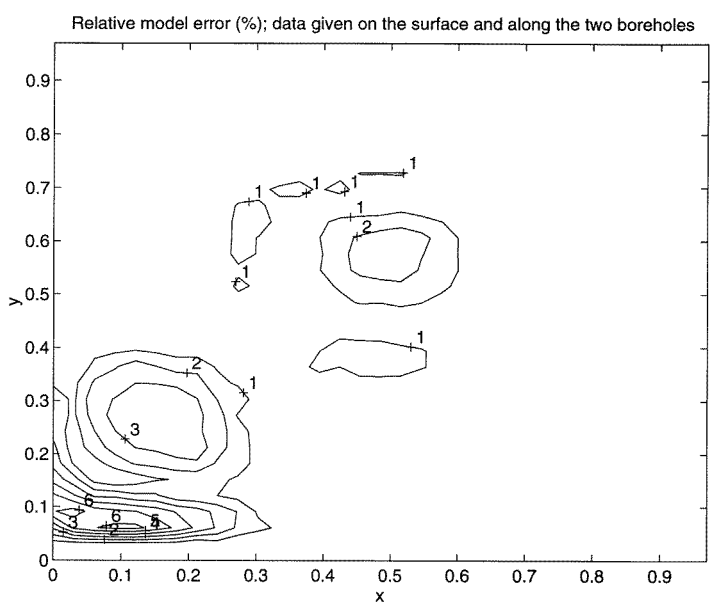

Figure 7. Relative model error (%).

the position of the saddle point is expected to be easily recovered in experiments with high contrast. For low contrasts, flow channelling is weak so the position of the saddle is harder to recover. In figures 8 and 9, we show the evolution of the relative error in three parameters (ϵ, σ_b and x_s) obtained from two numerical experiments that assume contrasts 10^4 and 14, respectively. As expected, when the contrast is high, the position of the saddle and the uniform background are recovered more quickly than the parameter ϵ that controls

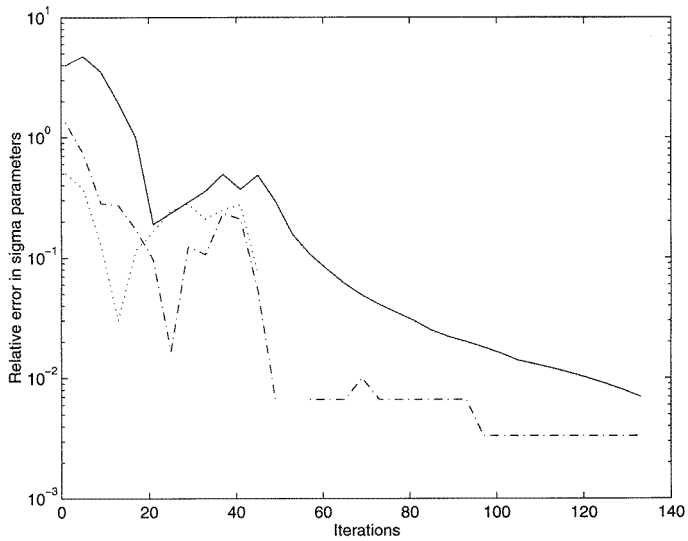

Figure 8. Convergence of high-contrast module parameters. Contrast of $\sigma = 10^4$. ——, ϵ; — · —, x_s; · · · · · ·, σ_b.

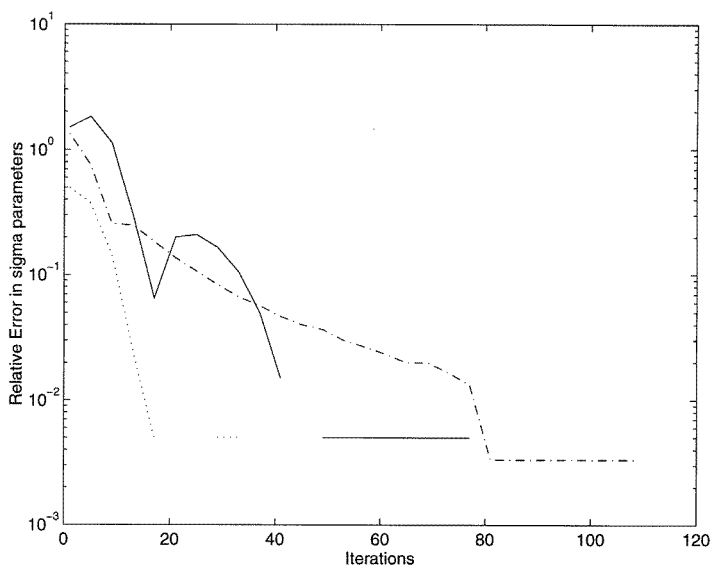

Figure 9. Convergence of high-contrast module parameters. Contrast of $\sigma = 14$. ——, ϵ; — · —, x_s; · · · · · ·, σ_b.

the contrast. However, when the contrast is lowered to 14 the position of the saddle is the last parameter to be recovered. The numerical experiment for reconstructing the model conductivity shown in figure 2 was repeated with data to which 5% noise has been added. The noise is simulated with independent, identically distributed Gaussian random variables. The starting point in the iteration is as before (see figure 3). From figure 10 we see that the mean-square error decreases to about 10^{-2} in 50 iterations and remains unchanged after that.

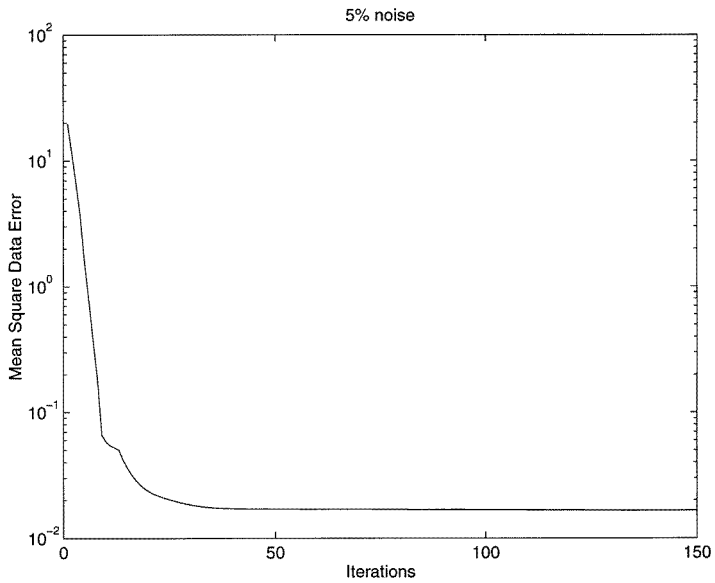

Figure 10. Evolution of mean-square data error (5% noise).

The relative error in the model in the L_∞ norm, shown in figure 11, tells us that, even with very noisy data, the algorithm recovers very well the background conductivity, the position and orientation of the channel and the support of the high contrast region. The error is high ($\sim$ 30%) only around the maxima of the conductivity where the potential gradient is nearly zero and so the inverse problem is ill-posed in this region. The quality of the results improves when the noise level is reduced. For example, with 1% noise the relative model error is smaller than 10%.

Since data are given only at a discrete number of points on the boundary, the resolution of the estimates is limited. To illustrate this point, we present the results of a numerical experiment with model conductivity in a tight, high-contrast configuration. If the domain is discretized with a uniform mesh corresponding to the number of data points on the boundary, the distance between the two maxima of the high-contrast conductivity is just six grid spacings. The contrast is 300 and the iteration starts, as before, with an initial guess that is far from the model parameters. The relative error in the conductivity at the end of the iteration process is shown in figure 12. Thus, the algorithm is successful in recovering the uniform background, the position and orientation of the channel, and the support of the high-contrast region, but it does not give a very accurate conductivity around the position of the maxima.

4.3. Non-uniform background

The numerical experiments presented so far show that the inversion algorithm described in section 3.1 is successful in imaging the conductivity when the model σ belongs to the same class of functions (4.1) within which we are searching. We now consider a more realistic experiment in which we try to recover the model conductivity shown in figure 13, which consists of a high-contrast module embedded in a variable background (see figure 14). The local variation in magnitude of the conductivity around the high-contrast region is about 100, but only about 7 elsewhere in the domain. The data (ϕ at the boundary) are given at 32

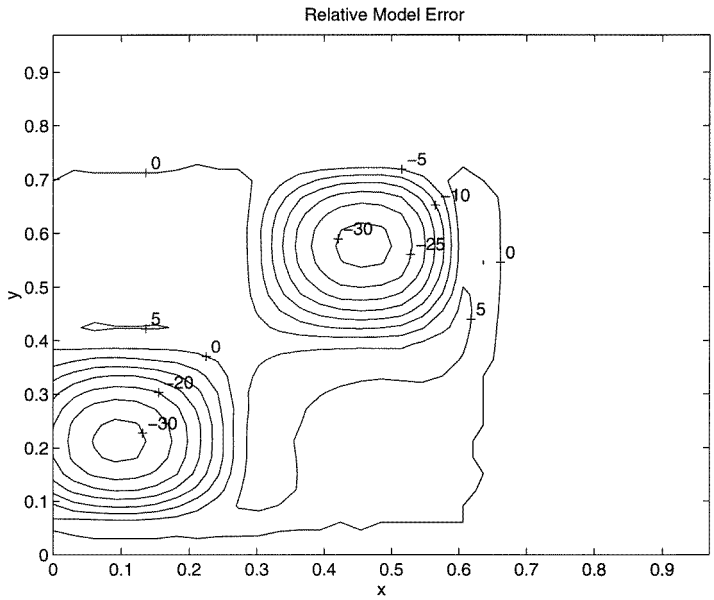

Figure 11. L_∞ conductivity error (5% noise).

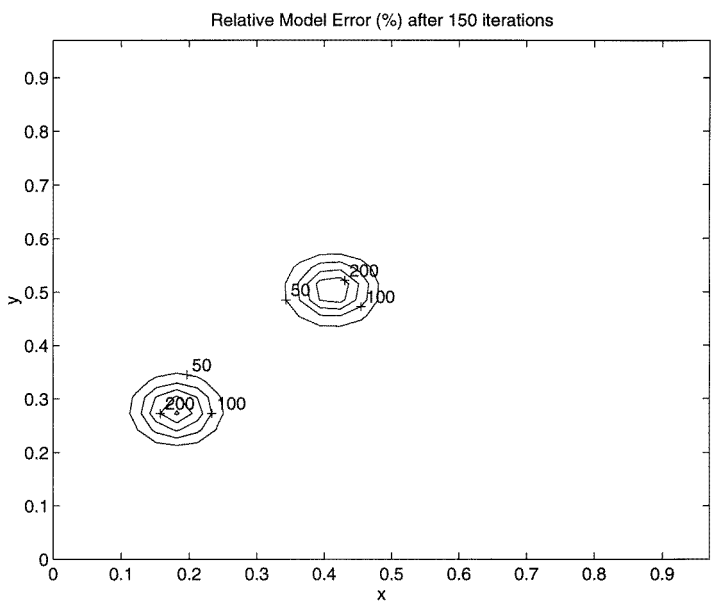

Figure 12. Tight high-contrast configuration.

uniformly distributed points along each side of the boundary and are generated numerically with the model conductivity shown in figure 13.

In the first step of the inversion process, we looked for a conductivity of the form (4.1) that fits the data best. In the computations we consider data generated with only two pairs of electrodes at $(0.0, 0.5), (1.0, 0.5)$ and $(0.5, 0.0), (0.5, 1.0)$, respectively. The result is shown in figure 15 and the error in the conductivity is shown in figures 16 and 17. Thus,

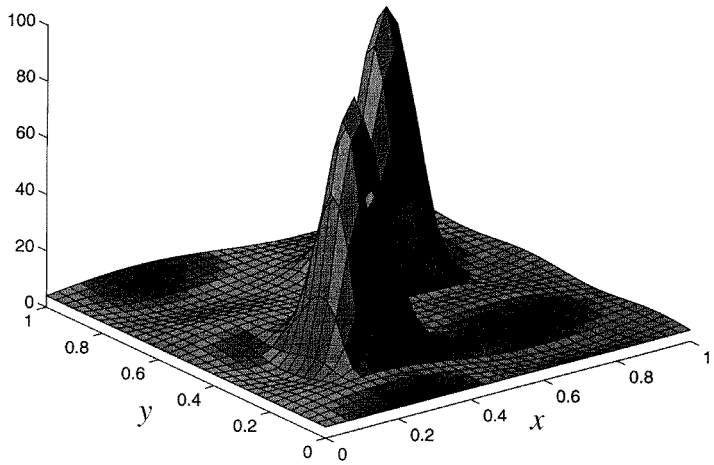

Figure 13. Model conductivity.

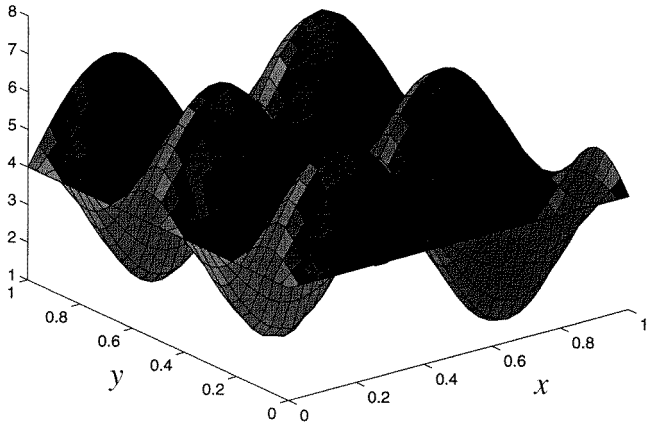

Figure 14. Background for the high-contrast module.

the inversion algorithm recovered the position and orientation of the channel as well as the support of the high-contrast region. The error is large around the two peaks of the conductivity and for the background in which we embedded the high contrast module. We may view the results of this first step as a low resolution image of the conductivity, that gives only features that control the leading-order term of the flow. Other details, like the variable background conductivity, are completely ignored.

In the second step of the inversion process, we improve the quality of the image by linearizing about the conductivity given in the first step. In the numerical computations, we use the same data points as before and many more pairs of electrodes for current injection. It is natural that in the first step of the inversion it is sufficient to consider data from only a few (two) current source–sink pairs while in the next step (the linearization process) we need data from many more current source–sink pairs. This simplification follows because the first inversion step looks only for the single channel of strong flow and, therefore, has only a few parameters to determine, while ignoring all other details of the conductivity. Thus, in order to get the single resistor in the asymptotic network, along with its position

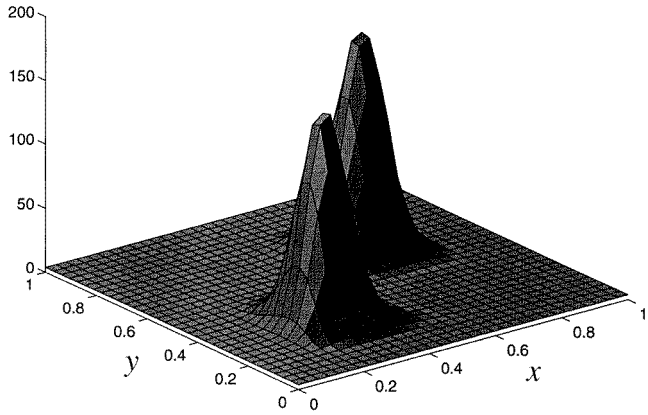

Figure 15. Conductivity after the first step of inversion.

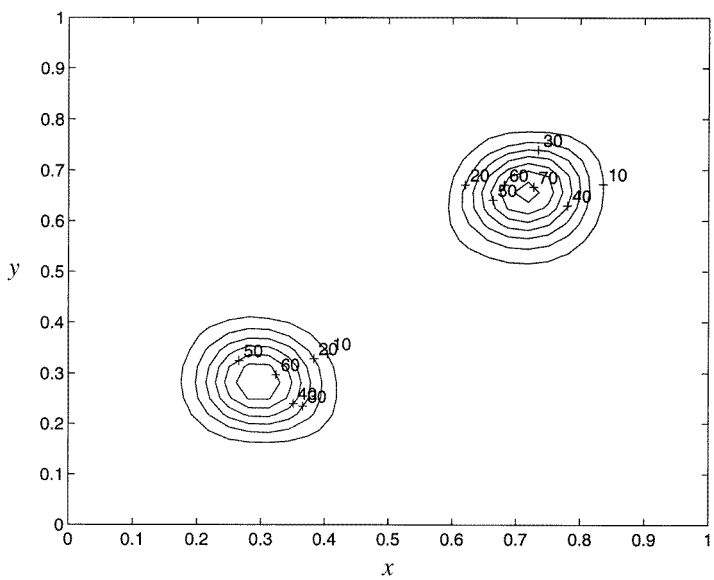

Figure 16. Absolute error in σ after the first step of the inversion.

and orientation, we only need two current source–sink pairs into the domain, chosen so that flow will cross it.

The relative error of the final conductivity (figure 18) shows clearly that the quality of the image has improved in the background, by almost 150%. It remains constant around the peaks in the high-contrast region of σ. The parameters identified in the first step of the inversion do not deteriorate during the linearization step.

4.4. Multiple channels

All the numerical examples presented so far have a single channel of flow concentration in the medium. In general, there can be an arbitrary number of unknown channels. Identification of the resistor network in these cases can be done with the algorithm described

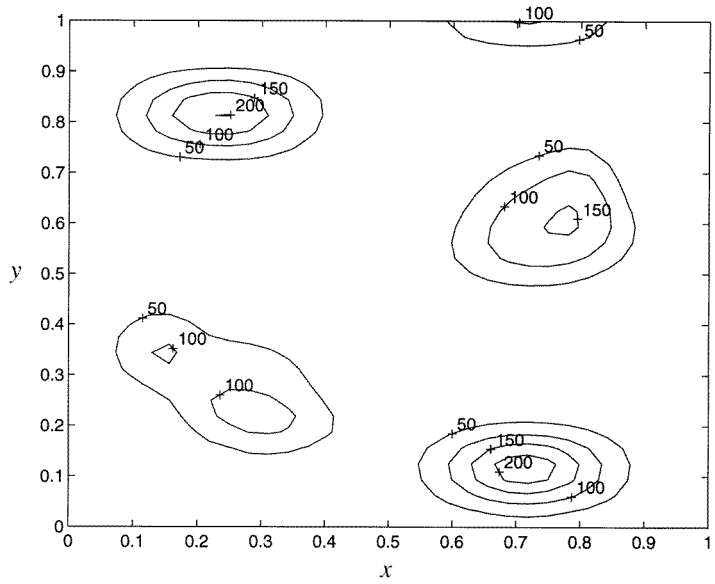

Figure 17. Relative error (%) in σ after the first step of the inversion.

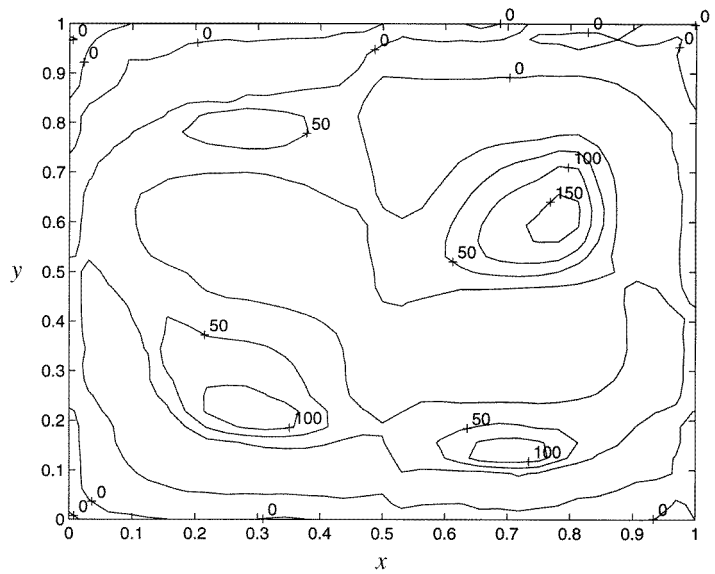

Figure 18. Relative error (%) in final σ.

before (section 3.1), where the model conductivity will have many high-contrast modules. Another approach is to identify a single channel at a time. We use this approach in imaging the conductivity of media with two and three channels of flow. If the channels are well separated, the algorithm works well. The channels are found sequentially, one by one, starting with the one closest to the boundary and ending with the ones in the interior of the flow domain.

The amount of data needed for inversion is larger than for media with a single channel

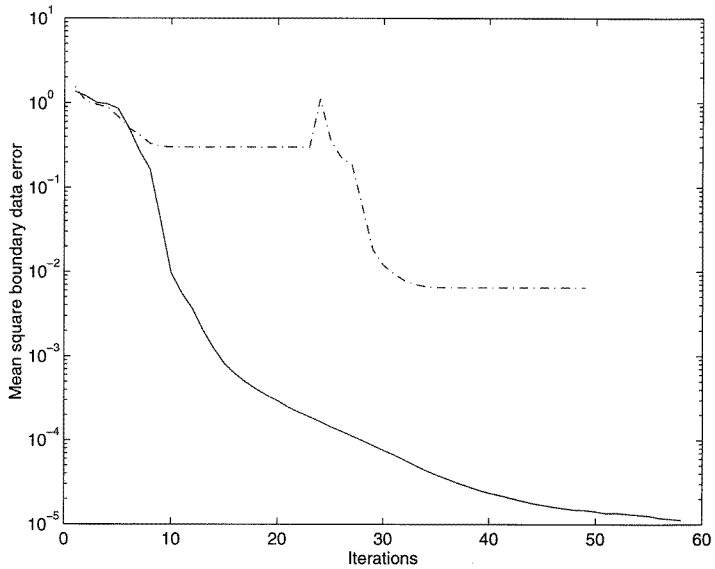

Figure 19. Output least-squares error as a function of the number of iterations. The full curve is for conductivity function with one high-contrast region. The dashed–dotted curve is for a conductivity with two high-contrast regions.

of flow concentration, where data from two source–sink pairs are sufficient. For instance, in a numerical experiment with two channels we can recover the resistor network with six source–sink pairs. The error in the boundary data is shown with the dashed–dotted curve in figure 19. The full curve represents the error in an experiment with the same conductivity minus the interior channel and the same amount of data. We see that the error for the experiment with a single channel drops to 10^{-5}, while the error in the experiment with two channels has a more complex behaviour. Initially, it decreases but then it stabilizes to a plateau at about 10^{-1}. This indicates that the algorithm has found the first channel and it cannot make any further reduction to the error unless a second high-contrast module is introduced. The insertion of the second module is identified by the slight peak observed in the error around iteration 25. After this introduction, the error drops rapidly and then stabilizes at about 10^{-3}, which indicates that the second channel has been identified. The error is worse than for the one-channel experiment but it can be reduced by using more data.

The numerical experiments of this section show that when the medium consists of well separated channels of flow concentration, they can be identified one by one in a manner very similar to the method of matching pursuit [36]. However, when the channels are close together the algorithm breaks down because it tries to fit a high-contrast module in between the channels. Such cases require special attention and will be considered in future research.

5. Physical interpretation of single-channel inversion

In this section we explain why the inversion method of section 3 is successful in finding the channels of flow inside the medium. We do this by identifying features in the boundary data that have channel information. We assume that the medium has a single channel and a conductivity that belongs to the class described by (4.1). The channel is oriented in the

vertical direction and is located at $(0.7, 0.6)$ (see figure 20). The asymptotic theory (see section 2.2) shows that the flow is concentrated around the channel and is diffuse elsewhere in the flow regime. Thus, when the boundary excitation is such that flow must pass through the channel, the potential gradient near it is a Gaussian centred at the saddle point and oriented in the vertical direction. The flow concentration in the interior of the medium is visible at those parts of the boundary that are relatively close to the channel.

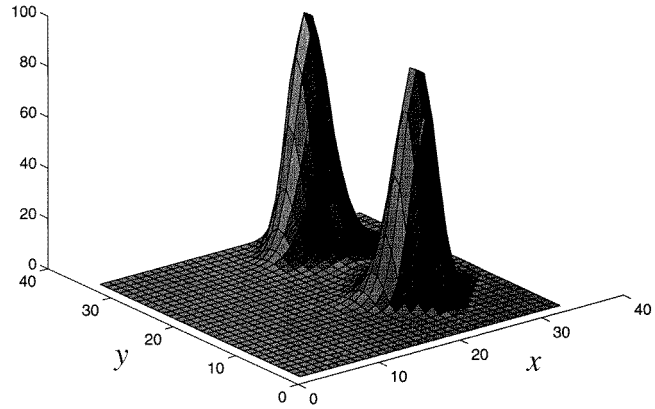

Figure 20. Conductivity with a vertical channel and uniform background.

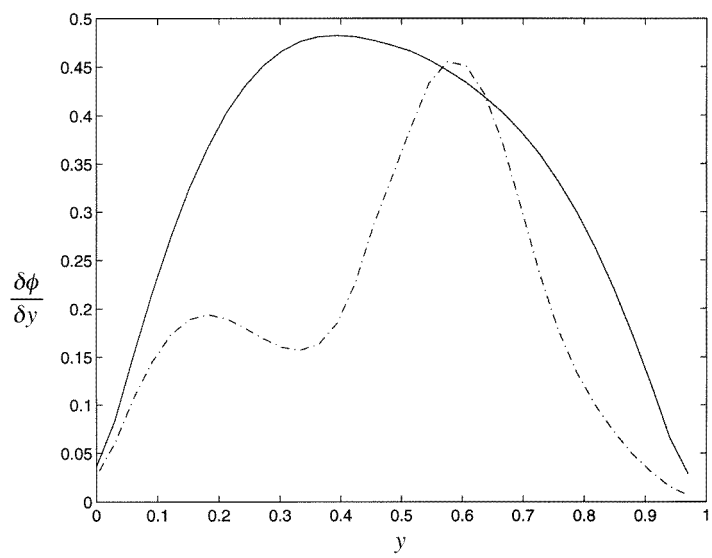

Figure 21. Vertical potential gradient at the left and right boundaries of Ω; ——, left boundary; — · —, right boundary.

For a current source located at (0.5, 0.0) and a sink at (0.5, 1.0), we plot in figure 21 the vertical potential gradient at the left and right boundaries of Ω. At the right boundary, which is closer to the saddle point, there is a maximum of the vertical potential gradient $(\nabla\phi \cdot \boldsymbol{e}_2)$ at $y = 0.6$. However, at the left boundary, which is farther away from the channel, flow concentration is not visible. When we drive the flow along the horizontal direction

(source and sink are located at (0.0, 0.5) and (1.0, 0.5), respectively), the channel rejects the flow. Thus, the horizontal potential gradient has a minimum near the saddle point, which can be seen at the top boundary around $x = 0.7$ (see figure 22). However, the minimum of $\nabla\phi \cdot \boldsymbol{e}_1$ cannot be observed at the bottom boundary, which is too far away from the channel. Thus, we can locate the vertical channel at $\boldsymbol{x}_S = (0.7, 0.6)$ very easily by just inspecting the boundary data.

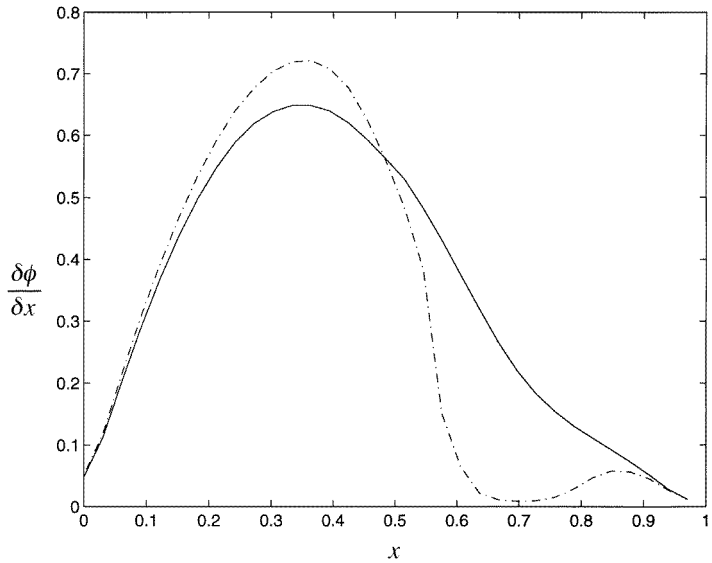

Figure 22. Horizontal potential gradient at the top and bottom boundaries of Ω; ——, bottom boundary; — · —, top boundary.

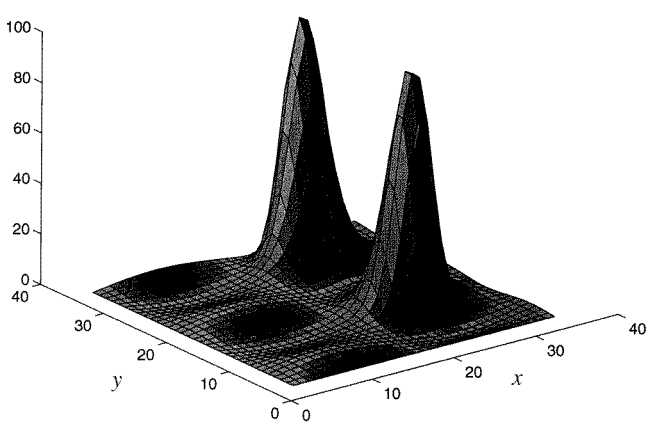

Figure 23. Conductivity with a vertical channel and variable background.

The picture is more complicated when the high-contrast module is embedded in a variable background because there are also regions of weak flow concentration in Ω that are felt at the boundary. For example, consider a medium with conductivity shown in figure 23. For a flow driven vertically with a current source and sink located at (0.5, 0.0) and (0.5, 1.0), respectively, the vertical potential gradient ($\nabla\phi \cdot \boldsymbol{e}_2$) at the right and

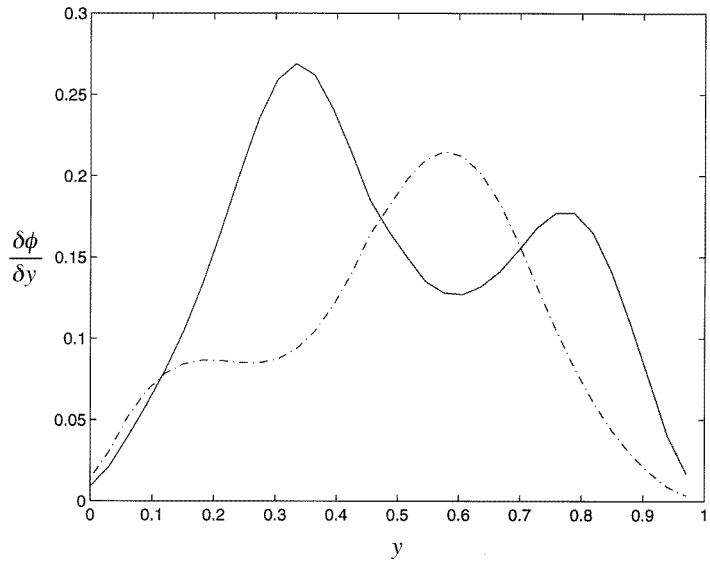

Figure 24. Vertical potential gradient at the left and right boundaries of Ω; ——, left boundary; — · —, right boundary.

left boundaries is shown in figure 24. At the right boundary, we observe three maxima of the vertical potential gradient: one is centred at the saddle point ($y = 0.6$) and the others (due to the minima of σ at (0.75, 0.12) and (0.83, 0.85)) are centred at $y = 0.12$ and $y = 0.85$, respectively. At the left boundary, which is far from the saddle point, the channel is invisible but we observe two maxima of $\nabla\phi \cdot \boldsymbol{e}_2$. These maxima are due to the minima of the conductivity located at (0.15, 0.31) and (0.15, 0.75), respectively. When the sources are moved to (0.0, 0.5) and (1.0, 0.5), so that the flow has a horizontal direction, the channel at $\boldsymbol{x}_S = (0.7, 0.6)$ rejects the flow. In figure 25 we show the horizontal potential gradient ($\nabla\phi \cdot \boldsymbol{e}_1$) at the top and bottom boundaries. The top boundary is closer to the channel and the minimum of $\nabla\phi \cdot \boldsymbol{e}_1$ at $x = 0.7$ is evident. However, although the channel is not seen at the bottom boundary, we nevertheless observe the maxima of the horizontal potential gradient that are due to the minima of σ located at (0.15, 0.31) and (0.75, 0.15).

In general, the conductivity of the unknown medium has a complicated structure and finding its main features in the interior of Ω by inspection of the boundary data would be nearly impossible. Regions of weak flow concentration could give misleading information and channels can be hidden from the boundary. Consequently, the heuristic method for identifying channels in the medium described in this section is, in general, inefficient and inaccurate for complex situations. The simple examples presented here give, however, a physical explanation for the success of the inversion algorithm of section 4 in localizing the channels in the medium.

6. Summary

We have introduced an inversion algorithm for tomographic imaging of media with large variations in the conductivity. The algorithm is based on the results of an asymptotic analysis of the forward problem in media with high contrast. This analysis shows that when the contrast of the conductivity is high, the flow can be roughly approximated by that of

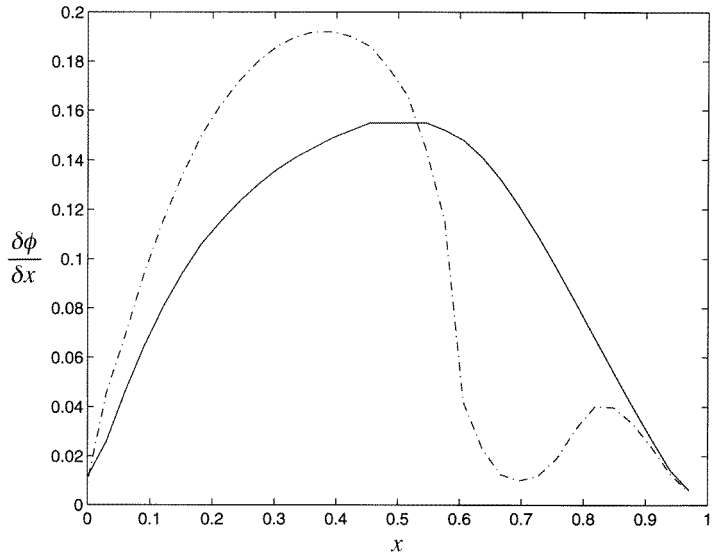

Figure 25. Horizontal potential gradient at the top and bottom boundaries of Ω; ——, bottom boundary; — · —, top boundary.

a resistor network. The network accounts for the main part of the flow and neglects the residual low-contrast features of the conductivity. We introduce a new parametrization of the conductivity based on the resistor network theory and use an output least-squares approach for identifying the network. We have shown that this parametrization acts as a regularization for the inverse problem. The conductivity estimated in this first stage of the algorithm is used as a reference conductivity in a second stage, where we identify low-contrast features that are not captured by the network.

We have assessed the performance of the algorithm with several numerical experiments and have shown that it is stable and successful in imaging high-contrast conductivities in many situations. At present, the inversion algorithm uses high-contrast modules that are somewhat rigid (see (4.1)–(4.5)), in the sense that they require the peaks of the conductivity surrounding the channel to have the same height. We are currently exploring less rigid models in order to eliminate this deficiency. Media with multiple channels of flow need to be explored further.

Acknowledgments

We thank F Natterer for several useful discussions and for pointing out the use of adjoint representations for solving (3.14). The work of J Berryman was performed under the auspices of the US Department of Energy by the Lawrence Livermore National Laboratory under contract No W-7405-ENG-48 and supported in part by the Geosciences Research Program of the DOE Office of Energy Research within the Office of Basic Energy Sciences, Division of Engineering and Geosciences. It was also supported in part by AFOSR grant F49620-94-1-0436. The work of L Borcea and G Papanicolaou was supported by NSF grant DMS96-22854 and AFOSR grant F49620-94-1-0436.

References

[1] Allen A and Santosa F 1991 Stability and resolution analysis of a linearized problem in electrical impedance tomography *Inverse Problems* **7** 515–33

[2] Alessandrini G 1988 Stable determination of conductivity by boundary measurements *Appl. Anal.* **27** 153–72

[3] Alumbaugh D L and Morrison H F 1993 Electromagnetic conductivity imaging with an iterative Born inversion *IEEE Trans. Geosci. Remote Sensing* **31** 758–63

[4] Alumbaugh D L and Morrison H F 1995 Monitoring subsurface changes over time with cross-well electromagnetic tomography *Geophys. Prospecting* **43** 873–902

[5] Bank E R 1990 *PLTMG: A Software Package for Solving Elliptic Partial Differential Equations* (Philadelphia, PA: SIAM)

[6] Banks T H and Kunisch K 1989 *Estimation Techniques for Distributed Parameter Systems* (Boston: Birkhaüser)

[7] Barber D and Brown B 1986 Recent developments in applied potential tomography-APT *Information Processing in Medical Imaging* ed S Bacharach (Amsterdam: Nijhoff) pp 106–21

[8] Bensoussan A, Lions J L and Papanicolaou G C 1978 *Asymptotic Analysis for Periodic Structures* (Amsterdam: North-Holland)

[9] Berryman J G 1990 Stable iterative reconstruction algorithm for nonlinear traveltime tomography *Inverse Problems* **6** 21–42

[10] Berryman J G 1989 Weighted least-squares criteria for seismic traveltime tomography *IEEE Trans. Geosci. Remote Sensing* **27** 302–9

[11] Berryman J G 1989 Fermat's principle and nonlinear traveltime tomography *Phys. Rev. Lett.* **62** 2953–6

[12] Berryman J G 1991 Convexity properties of inverse problems with variational constraints *J. Franklin Instit.* **328** 1–13

[13] Borcea L and Papanicolaou G C 1996 Network approximation for transport properties of high contrast materials *SIAM Appl. Math.* at press

[14] Borcea L and Papanicolaou G C 1996 A hybrid numerical method for high contrast conductivity problems *J. Comput. Appl. Math.* submitted

[15] Borcea L, Papanicolaou G C and Wehr J Network approximation for high contrast random conductivities, in preparation

[16] Curtis E B and Morrow J A 1990 Determining the resistors in a network *SIAM J. Appl. Math.* **50** 931–41

[17] Daily W D, Ramirez D, LaBreque D and Nitao J 1992 Electrical resistivity tomography of vadose water movement *Water Resources Res.* **28** 1429–42

[18] Dennis J E and Schnabel R B 1996 *Numerical Methods for Unconstrained Optimization and Nonlinear Equations* (Philadelphia, PA: SIAM)

[19] Dines K A and Lytle R J 1981 Analysis of electrical conductivity imaging *Geophysics* **46** 1025–36

[20] Fletcher R 1987 *Practical Methods of Optimization* (New York: Wiley)

[21] Gill P E, Murray W and Wright M H 1981 *Practical Optimization* (London: Academic)

[22] Habashy T M, Groom R W and Spies B R 1993 Beyond the Born and Rytov approximations: a nonlinear approach to electromagnetic scattering *J. Geophys. Res.* **98** 1759–55

[23] Hestenes M R and Stiefel E 1952 Methods of conjugate gradients for solving linear systems *J. Res. NBS* **49** 409–36

[24] Isakov V 1993 Uniqueness and stability in multi-dimensional inverse problems *Inverse Problems* **9** 579–621

[25] Ito K and Kunisch K 1990 The augmented Lagrangian method for parameter estimation in elliptic systems *SIAM J. Control* **28** 113–36

[26] Jikov V V, Kozlov S M and Oleinik O A 1994 *Homogenization of Differential Operators and Integral Functional* (Berlin: Springer)

[27] Kaczmarz S 1937 Angenäherte auflösung von systemen linearer gleichungen *Bull. Acad. Polon. Sci. Lett.* A **35** 355–7

[28] Kitanidis P K 1995 Quasilinar geostatistical theory for inversing *Water Resources Res.* **31** 2411–19

[29] Kohn R and Vogelius M 1985 Determining conductivity by boundary measurements *Commun. Pure Appl. Math.* **38** 643–67

[30] Kozlov S M 1989 Geometric aspects of averaging *Russian Math. Surveys* **44** 91–144

[31] 1992 *LAPACK User's Guide* (Philadelphia, PA: SIAM)

[32] Levenberg K 1944 A method for the solution of certain non-linear problems in least squares *Q. Appl. Math.* **2** 164–8

[33] Lu Shin-yee and Berryman J G 1990 Inverse scattering, seismic traveltime tomography, and neural networks *Int. J. Imaging Syst. Technol.* **2** 112–18

[34] Marquardt D W 1963 An algorithm for least-squares estimation of nonlinear parameters *SIAM J. Appl. Math.* **11** 431–41
[35] Marquardt D W 1970 Generlized inverses, ridge regression, biased linear estimation, and nonlinear estimation *Technometrics* **12** 591–612
[36] Mallat S and Zhang Z 1993 Matching pursuit in a time-frequency dictionary *IEEE Trans. Signal Process.* **41** 3397–415
[37] McCormick S F and Wade J G 1993 Multigrid solution of a linearized, regularized least-squares problem in electrical impedance tomography *Inverse Problems* **9** 697–713
[38] Mitchell A R 1969 *Computational Methods in Partial Differential Equations* (New York: Wiley)
[39] Natterer F 1986 *The Mathematics of Computerized Tomography* (New York: Wiley)
[40] Ramirez A, Daily D W, LaBrecque D, Owen E and Chesnut D 1993 Monitoring an underground steam injection process using electrical resistance tomography *Water Resources Res.* **29** 73–87
[41] Rector J W (ed) 1995 *Geophysics* **60** Specal issue on Crosswell methods
[42] Santosa F and Vogelius M 1990 A backprojection algorithm for electrical impedance imaging *SIAM J. Appl. Math.* **50** 216–43
[43] Sylvester J and Uhlmann G 1987 A global uniqueness theorem for an inverse boundary value problem *Ann. Math.* **125** 153–69
[44] Sylvester J and Uhlmann G 1990 The Dirichlet to Neumann map—and applications *Inverse problems in Partial Differential Equations* ed D Colton, R Ewing and W Rundell (Philadelphia, PA: SIAM) pp 101–39
[45] Tikhonov A and Arsénine V 1976 *Méthodes de Résolution de Problèmes Mal Posés* (Moscow: Mir)
[46] Yorkey T J, Webster J G and Tompkins W J 1987 Comparing reconstruction algorithms for electrical impedance tomography *IEEE Trans. Biomed. Engng* **34** 843–52
[47] Zhou Q, Becker A and Morrison H F 1993 Audio-frequency electromagnetic tomography in 2-D *Geophysics* **58** 482–95